PNAS RESEARCH ARTICLE | GENETICS

Inactive PARP1 causes embryonic lethality and genome instability in a dominant-negative manner

Zhengping Shao[a], Brian J. Lee[a], Hanwen Zhang[a], Xiaohui Lin[a], Chen Li[a], Wenxia Jiang[a], Napon Chirathivat[b,c,d,e], Steven Gershik[a], Michael M. Shen[b,c,d,e], Richard Baer[a,f], and Shan Zha[a,f,g,h,1]

Edited by Sue Jinks-Robertson, Duke University School of Medicine, Durham, NC; received February 3, 2023; accepted June 13, 2023

PARP1 (poly-ADP ribose polymerase 1) is recruited and activated by DNA strand breaks, catalyzing the generation of poly-ADP-ribose (PAR) chains from NAD+. PAR relaxes chromatin and recruits other DNA repair factors, including XRCC1 and DNA Ligase 3, to maintain genomic stability. Here we show that, in contrast to the normal development of Parp1-null mice, heterozygous expression of catalytically inactive Parp1 (E988A, *Parp1*$^{+/A}$) acts in a dominant-negative manner to disrupt murine embryogenesis. As such, all the surviving F1 *Parp1*$^{+/A}$ mice are chimeras with mixed *Parp1*$^{+/AN}$ (neoR retention) cells that act similarly to *Parp1*$^{+/-}$. Pure F2 *Parp1*$^{+/A}$ embryos were found at Mendelian ratios at the E3.5 blastocyst stage but died before E9.5. Compared to *Parp1*$^{-/-}$ cells, genotype and expression-validated pure *Parp1*$^{+/A}$ cells retain significant ADP-ribosylation and PARylation activities but accumulate markedly higher levels of sister chromatid exchange and mitotic bridges. Despite proficiency for homologous recombination and nonhomologous end-joining measured by reporter assays and supported by normal lymphocyte and germ cell development, *Parp1*$^{+/A}$ cells are hypersensitive to base damages, radiation, and Topoisomerase I and II inhibition. The sensitivity of *Parp1*$^{+/A}$ cells to base damages and Topo inhibitors exceed *Parp1*$^{-/-}$ controls. The findings show that the enzymatically inactive PARP1 dominant negatively blocks DNA repair in selective pathways beyond wild-type PARP1 and establishes a crucial physiological difference between PARP1 inactivation vs. deletion. As a result, the expression of enzymatically inactive PARP1 from one allele is sufficient to abrogate murine embryonic development, providing a mechanism for the on-target side effect of PARP inhibitors used for cancer therapy.

PARP1 | PARP inhibitor | inactivation | embryonic | DNA damage

PARP1 belongs to the family of poly-ADP ribose polymerases (PARPs) that share a conserved ADP-ribose (ADPr) transferase (ART) domain. PARP1 and the related PARP2 are recruited to DNA strand breaks, where they are activated to catalyze the transfer of the ADP-ribose to the protein substrate (mono-ADP-ribosylation, MARylation) and then chain extension (Poly-ADP-ribosylation, PARylation) to form poly-ADP-ribose (PAR). PAR promotes chromatin relaxation and recruits other repair proteins, including the XRCC1-Ligase3 complex that ligates single-strand DNA nicks, such as those generated during base excision repair (BER) (1–3). PARP1 is more abundant than PARP2, has a higher affinity for diverse DNA lesions, and accounts for >80% of DNA damage-induced PARP activity (4). Yet, *Parp1*-null mice are viable, fertile, and of standard size (5). Indeed, the use of PARP enzymatic inhibitors (PARPi) for cancer therapy is based not only on the extreme sensitivity of BRCA1- or BRCA2-deficient cancer cells to PARP1 loss, but also on the nonessential role of PARP1 in normal tissues (6, 7).

In addition to blocking its enzymatic activity, PARPi also induces a phenotype termed "PARP trapping", characterized by the persistence of damage-induced PARP1/2 foci and prolonged retention of PARP1/2 on damaged chromatin (8–11). Loss of PARP1, but not PARP2, causes marked resistance to PARP inhibitors (10, 11), highlighting the unique importance of PARP1 inhibition in cancer therapy. Several mechanisms have been proposed to explain PARP1 trapping (12). In vitro, PARPi prevents PARP1 auto-PARylation, which correlates with the release of PARP1 from DNA ends (9). But this mechanism alone cannot explain why PARPi with similar IC50s for enzymatic inhibition have different abilities to "trap" PARP1. Structural analyses later showed that the nonhydrolyzable NAD+ analog benzamide adenine dinucleotide could reverse-allosterically enhance PARP1 affinity for DNA ends (13), providing an explanation for the differential trapping by inhibitors with distinct chemical structures. PARPi attenuates PAR, which recruits XRCC1-LIG3 and other repair complexes (11). Using quantitative live-cell imaging, we recently showed that PARP1 molecules exchange rapidly at microirradiation sites in cells (11), even in the presence of clinically effective PARPi, suggesting that the PARPi-induced persistence of

Significance

PARP1 (poly-ADP ribose polymerase 1) is the primary target of PARP enzymatic inhibitors. Therapeutic use of PARP inhibitors for cancer is based on not only the extreme sensitivity of BRCA1/2-deficient cancer cells to PARP1 inhibition but also the nonessential role of PARP1 in normal tissues. Here, we show that in contrast to the normal development of Parp1-null mice, the mouse model heterozygously expressing the catalytically inactive Parp1 (E988A, *Parp1*$^{+/A}$) dies embryonically with high levels of genomic instability. The results reveal the severe dominant-negative impact of catalytically inactive PARP1, indicating the presence of enzymatically inactive PARP1 is much more damaging to normal tissues than previously anticipated. These findings provide a mechanism for clinical PARP inhibitors' unexpected normal tissue toxicity.

Author contributions: Z.S. and S.Z. designed and performed most research; B.J.L. performed proliferation analyses, HR and NHEJ reporter assay, and supported mouse genetic work; H.Z. helped with cellular experiments and data analyses; X.L. conducted RT-PCR analyses and pan-ADP-ribosylation analyses; C.L. and W.J. generated Parp1-E988A and Parp1 conditional knock-out alleles; N.C. and M.M.S. helped with mouse early embryonic development analyses; S.G. provided support for the animal work; and Z.S., R.B., and S.Z. wrote the paper.

The authors declare no competing interest.

This article is a PNAS Direct Submission.

[1]To whom correspondence may be addressed. Email: sz2296@cumc.columbia.edu.

This article contains supporting information online at https://www.pnas.org/lookup/suppl/doi:10.1073/pnas.2301972120/-/DCSupplemental.

Published July 24, 2023.

PARP1 foci may reflect continual recruitment of different PARP1 molecules to the unrepaired DNA lesion due to delayed repair. In this regard, the release and exchange of PARP1 from model DNA ends in vitro can also occur independently of auto-PARylation and in the presence of clinically relevant PARPi (12, 14–16).

Although the therapeutic effects of PARP inhibition and trapping on tumor cells have been studied extensively, less is known about the impact of inactive PARP1 on normal cells, despite accumulating evidence of clinical PARPi toxicities in patients as hematological and gastric-intestinal toxicities, and inhibitor-treated mouse models as acute hematological toxicities (17–20). To address this question and understand the physiological impact of inactive PARP1 protein, we introduced a catalytically inactive point mutation into the endogenous Parp1 locus. Here we show that, in contrast to the normal development of Parp1-null mice, heterozygous expression of catalytically inactive Parp1 (E988A, *Parp1*$^{+/A}$) acts in a dominant-negative manner to disrupt embryogenesis and genome stability. *Parp1*$^{+/A}$ cells are characterized by the elevated formation of mitotic bridges and sister chromatid exchanges (SCEs). The genome toxicity is due to the accumulation of inactive PARP1 protein at DNA damage sites, but not the loss of ADP-ribosylation and PARylation activity. Mechanistically, we show that inactive PARP1-E988A is recruited to DNA damage sites where it forms persistent foci. Especially, the inactive Parp1 blocks the resolution of DNA damage induced by alkylating agents and topoisomerase inhibitors beyond the loss of PARP1, but not clean DNA double-strand break (DSB) repair via homologous recombination (HR) or nonhomologous end-joining (NHEJ), measured by lymphocyte development, meiosis, and reporter assays. The results demonstrate a clear difference between PARP1 inhibition vs. PARP1 deletion on normal tissues, providing the molecular mechanism for the initially unexpected and significant adverse effects of PARPi.

Results

The Generation and Characterization of Catalytically Inactive Parp1 Murine Model. To address the impact of inactive PARP1 on normal issue, we generated the *Parp1*^{AN} allele by introducing the catalytically inactive E988A missense mutation (21) and an FRT-NeoR-FRT cassette into the endogenous Parp1 locus of mice (Fig. 1 *A* and *B*). The E988A mutation abrogates the PARylation activity of PARP1 without affecting its DNA binding (21) or MARylation activity at high NAD+ concentration (11). Since the

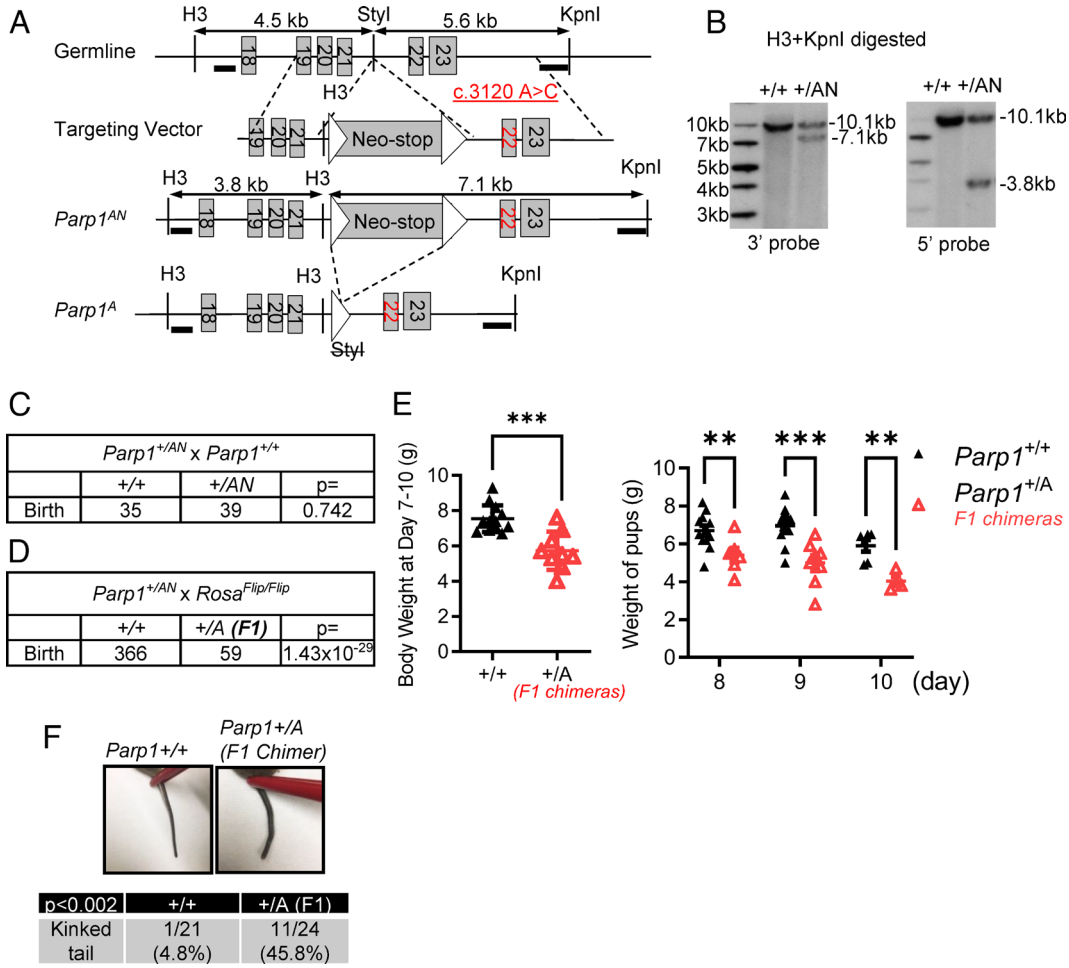

Fig. 1. Expression of catalytically inactive Parp1 impairs murine development. (*A*) Mouse Parp1 E988 E->A targeting strategy. The schematic diagram represents the murine Parp1 germline structure (top row), targeting vector (second row), targeted allele (Parp1^{AN}, third row), and the recombined E988A expression allele without neo (Parp1^{A}, bottom row). The presence of the NeoR in the Parp1^{AN} allele interferes with the expression of Parp1, resulting in no or little Parp1 expression. Map not shown to scale. (*B*) Southern blot analysis of targeted *Parp1* $^{+/AN}$ ES cell DNA using 5′ and 3′ probes. *Left*: wild-type ES cells. *Right*: targeted ES cells. Top band: germline. Lower band: targeted. (*C*) The birth rate of F1 pups from *Parp1*$^{+/AN}$ x *Parp1*$^{+/+}$ crossing. *P*-values were calculated via the χ^2 test. (*D*) The birth rate of F1 pups from *Parp1*$^{+/AN}$ x *Rosa*$^{Flip/Flip}$ crossing. *P*-values were calculated via the χ^2 test. (*E*) Body weight of day 7 to 10 *Rosa*$^{+/Flip}$ *Parp1*$^{+/A}$ and age-matched control *Rosa*$^{+/Flip}$ *Parp1*$^{+/+}$ littermate pups. The *Rosa*$^{+/Flip}$ *Parp1*$^{+/A}$ pups were consistently smaller in this age window. *P*-value was calculated using multiple student's *t* test. $^{**}P < 0.01$, $^{***}P < 0.001$. (*F*) Representative images and frequency of F1 *Parp1*$^{+/A}$ chimeras or *Parp1*$^{+/+}$ mice with kinked tails.

FRT-NeoR-FRT cassette blocks transcription (Fig. 1*A*), *Parp1*^{AN} behaves like a null allele and, as anticipated, *Parp1*$^{+/AN}$ pups were born at the expected Mendelian ratio (Fig. 1*C*). To remove the cassette and generate the desired *Parp1*^{A} allele, *Parp1*$^{+/AN}$ mice were bred with *Rosa*$^{FLIP/FLIP}$ mice that constitutively expresses the FLIPase from the blastocyte stage (E3.5) in widespread tissues including the reproductive organs (Jax Strain No. 003946 in 129Sv) (22, 23). Regardless of whether the *Rosa*$^{FLIP/FLIP}$ came from the paternal or the maternal side, the F1 *Parp1*$^{+/A}$ pups were significantly underrepresented among the progeny (1/6 of expected) (Fig. 1*D*). They were also ~25% smaller than their littermates at pre-weaning ages (Fig. 1*E*) and many (~45.8%) had kinked tails (Fig. 1*F*), a phenotype previously seen in genomic instability mouse models (e.g., *H2ax*$^{-/-}$ or *Brca1* mutants), but not in *Parp1*$^{-/-}$ mice, suggesting that catalytically inactive Parp1 polypeptides can disrupt genome integrity in a dominant-negative manner.

F2 *Parp1*$^{+/A}$ Mice Die during Early Embryonic Development. Curiously, all the F2 pups (n = 52) of mating between *F1 Parp1*$^{+/A}$ mice and WT partners (both genders) were *Parp1*$^{+/+}$, regardless of *Tp53* status(Fig. 2*A*, $P < 3.9 \times 10^{-9}$) and despite equal representation of *Parp1*^{E988A} and *Parp1*$^{+}$ alleles in the sperm of F1 *Parp1*$^{+/A}$ mice (Fig. 2*B*). Timed mating showed that F2 *Parp1*$^{+/A}$ embryos were recovered with normal early-stage blastocyst morphology at E3.5 (Fig. 2*C*) but could not be recovered at E9.5, indicating F2 *Parp1*$^{+/A}$ animals likely suffered early embryonic lethality (Fig. 2*A*). Moreover, despite the known requirement for HR in germ cell development and meiosis, testis architecture (Fig. 2*D*), sperm counts (Fig. 2*E*), testis weight (Fig. 2*F*), and sperm mobility were normal in young F1 *Parp1*$^{+/A}$ mice used for breeding (*SI Appendix*, Fig. S1*A*). The lack of F2 *Parp*$^{+/A}$ mice was perplexing given the viability of F1 *Parp1*$^{+/A}$ pups (Fig. 1*D*). We hypothesized that the surviving F1 *Parp1*$^{+/A}$ mice might be chimeras, which carry *Parp1*$^{+/AN}$ cells that had escaped FLIPase excision and whose presence, although low in frequency, support the embryogenesis of F1 *Parp1*$^{+/A}$ mice. To test this possibility, we regenotyped F1 *Parp1*$^{+/A}$ mice by PCR using both the standard triplex primers (detecting AN, A, and + alleles) as well as primers that only detect the AN allele (*SI Appendix*, Fig. S1*B*). All F1 *Parp1*$^{+/A}$ mouse tail DNAs tested AN-positive (allele frequency: 1% to 10%) in the AN-specific PCR assay (Fig. 2 *G* and *H* and *SI Appendix*, Fig. S1 *C* and *D*). We note that the PCR product for the A allele shares 230-bp sequence identical to that of the + allele, except the ~80-bp insertion corresponding to the FRT site and its surrounding sequence (*SI Appendix*, Fig. S1*B*). As a result, when both A and + products are present (e.g., in *Parp1*$^{+/A}$), the two PCR products sometimes form a heteroduplex that migrates between the WT and A PCR product (Fig. 2*G*). Moreover, qPCR analyses of peripheral blood from F1 *Parp1*$^{+/A}$ mice at different ages showed a progressive increase in AN allele frequency from ~1% at 3 wk to ~100% at 64 wk (Fig. 2*I*). This is consistent with the low chimerism in the tail DNA collected at 7 d after birth (Fig. 2 *G* and *H* and *SI Appendix*, Fig. S1 *C* and *D*). Thus, we concluded that pure heterozygosity abrogates the embryonic development of *Parp1*$^{+/A}$ mice.

Normal Lymphocyte Development and Spermatogenesis in Viable Young (<8 wk) F1 *Parp1*$^{+/A}$ Chimeric Mice. PARP1 is activated by DNA breaks. To understand the mechanism of growth retardation, we then asked whether inactive Parp1 blocks DNA DSB repair. Mammalian cells have two major DSB repair pathways –NHEJ and HR. Specifically, lymphocyte development requires the ordered assembly and subsequent modification of immunoglobulin (Ig) genes through two programmed DSB events–V(D)J recombination and Ig class switch recombination (CSR) (24). Defects in the NHEJ pathway abrogate V(D)J recombination and significantly impair CSR (24), serving as a physiological readout of NHEJ. The *Parp1*$^{+/AN}$ chimerism in the F1 *Parp1*$^{+/A}$ mice is consistently <10% in peripheral blood by 15 wk of age. So, we focused our analyses of the F1 Chimeric *Parp1*$^{+/A}$ on young mice only. Like in Parp1 null mice (5), B and T lymphocyte development measured by both relative frequency of immature and mature cells and developmental state-specific cellularity, were both normal in young F1 *Parp1*$^{+/A}$ mice (<8 wk) (Fig. 3 *A*–*C*). Representative genotype verified that AN allele frequency in the lymphoid organs is <=10% at the time of analyses (*SI Appendix*, Fig. S1*E*). Furthermore, IgH CSR, a sensitivity measure for NHEJ (25), was also normal in the splenocytes purified from young F1 *Parp1*$^{+/A}$ mice (<8 wk) (Fig. 3 *A* and *D*). Since CSR efficiency can be influenced by cell proliferation, we further measured CSR by gating cells with the same cell division. No measurable defects in CSR were noted in *Parp1*$^{+/A}$ splenocytes even after being controlled for cell division (*SI Appendix*, Fig. S2*A*). Given the normal spermatogenesis, a process that requires HR, in young *Parp1*$^{+/A}$ chimeras, these data together suggest that heterozygous expression of inactive PARP1 does not have a major impact on NHEJ or HR. However, due to the chimerism, although low, we would not be able to rule out minor impacts on HR and NHEJ in the *Parp1*$^{+/A}$ mice based on the apparent normal development in F1 chimeric *Parp1*$^{+/A}$ mice.

***Parp1*-E988A Forms Persistent Foci at Microradiation Sites without Exchange Defects.** To ascertain whether E988A extends the appearance of PARP1 at DNA damage sites, we measured the kinetics of foci formation by GFP-tagged PARP1 following 405-nm microirradiation in PARP1 knockout human osteosarcoma cell line—U2OS previously generated in our lab (11). We chose the PARP1 knockout cells to prevent the endogenous PARP1 from interfering with the dynamics of the GFP-tagged PARP1. U2OS is commonly used as a model for quantitively live cell imaging due to its flat nuclear shape, reliable and high transfection efficiency, and consistent behavior upon microirradiation. Both GFP-PARP1-E988A and GFP-PARP1-WT proteins rapidly formed foci within 1 min of irradiation, suggesting the E988A mutation does not affect DNA binding by PARP1 (Fig. 4 *A* and *B*). As expected, cells expressing GFP-PARP1-E988A failed to form bright PAR-dependent XRCC1 foci, consistent with the lack of PARylation activity (Fig. 4 *A* and *C* and *SI Appendix*, Fig. S2*B*). However, unlike GFP-PARP1-WT foci, which dissolved within ~10 min, at least 35% of GFP-PARP1-E988A foci persisted for 20 min and 25% lasted to 30 min (Fig. 4 *A* and *D*). The lack of XRCC1 foci formation and the persistent PARP1 foci in cells expressing PARP1-E988A are comparable to PARP inhibitor—niraparib-treated cells expressing PARP1 WT (Fig. 4 *A*–*D*). The presence of PARP1 E988A at the DNA ends in later time points could physically block the recruitment of other DNA repair factors, including PARP2 (see below).

Persistent PARP1 foci could be caused by allosteric trapping of the same PARP1 molecule at the DNA breaks or by continuous recruitment of different PARP1 molecules to the breaks due to the lack of repair (e.g., reduced PAR-dependent recruitment of the XRCC1-LIG3 complex) (11). To distinguish these two possibilities, we measured florescence recovery after photobleach (FRAP). Upon photobleaching, GFP-PARP1-E988A foci recovered as efficiently as the WT control (11) (Fig. 4 *E* and *F*), suggesting that E988A mutation does NOT affect the exchange of PARP1 at the DNA damage foci and the persistency of

A

Parp1$^{+/A}$ *(F1 chimeras) x Parp1*$^{+/+}$			
Parp1	*+/+*	*+/A (F2)*	p=
E3.5	25	21	0.67
E9.5	9	0	0.015
Birth	52	0	3.9E-09
Parp1$^{+/A}$ *(F1 Chimeras) x Tp53*$^{+/-}$			
Tp53	*Tp53+/-*		
Parp1	*+/+*	*+/A (F2)*	p=
Birth	38	0	4.8E-07

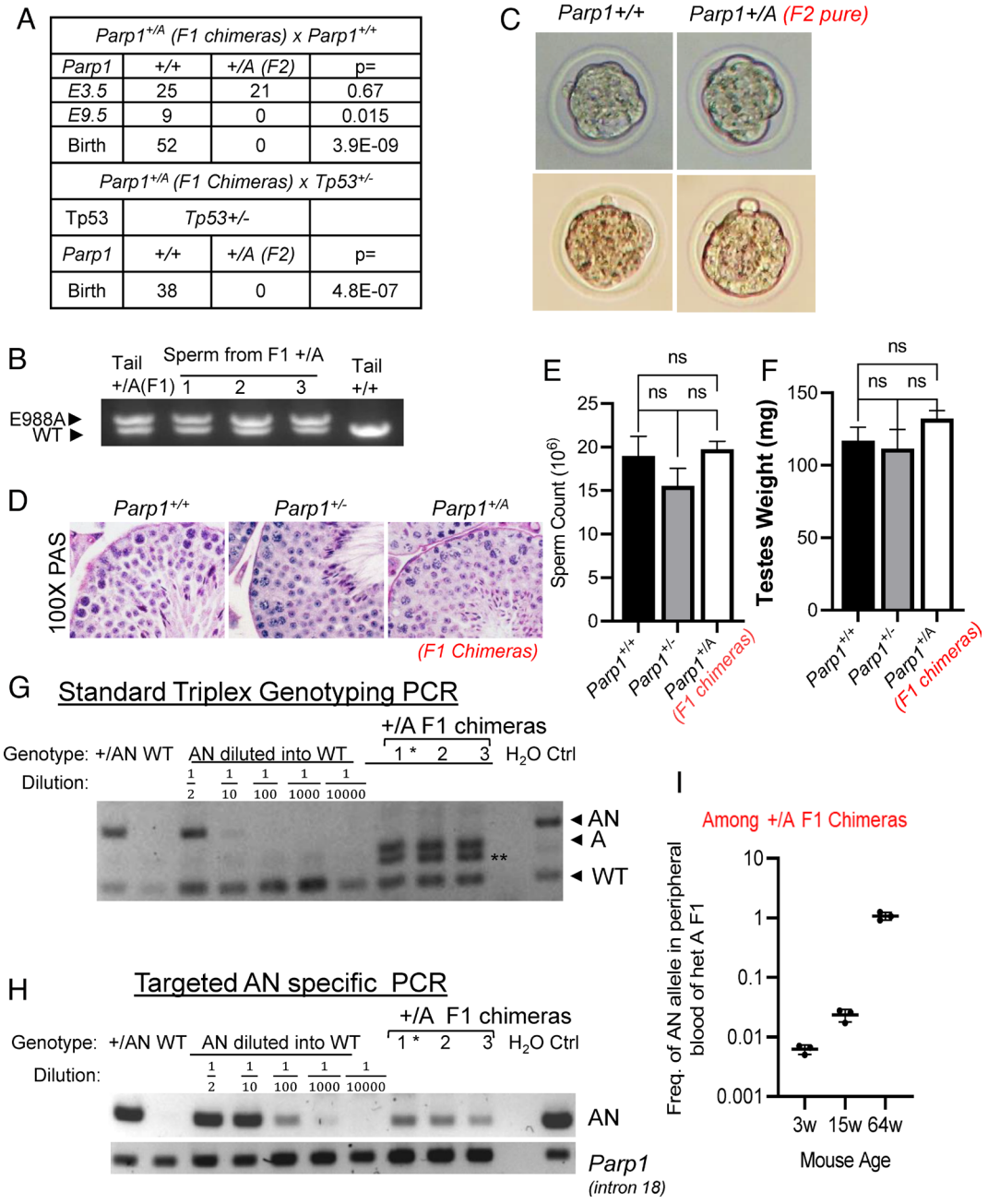

Fig. 2. Heterozygous expression of inactive Parp1-E988A causes embryonic lethality in mice. (*A*) The frequency of F1 *Parp1*$^{+/A}$ pups from *Parp1*$^{+/A}$ x *Parp1*$^{+/+}$ crossing with or without *Tp53* deficiency at different developmental stages. *P*-values were calculated via the χ^2 test. (*B*) PCR identification of *Parp1*^{A}allele in F1 *Parp1*$^{+/A}$ mice sperm. (*C*) Morphology of F2 *Parp1*$^{+/+}$ and *Parp1*$^{+/A}$ early-stage blastocysts at E3.5. (*D*) Histology with H&E staining showing spermatogenesis in young (<8 wk) male *Parp1*$^{+/+}$, *Parp1*$^{+/-}$, and *F1 Parp1*$^{+/A}$testes. (*E*) Epididymis mature sperm count of *Parp1*$^{+/+}$, *Parp1*$^{+/-}$, and *Parp1*$^{+/A}$ adult males. The *P*-value was calculated based on one-way ANOVA. ns: $P > 0.05$. (*F*) Testes weight from F1 *Parp1*$^{+/A}$and control male *Parp1*$^{+/+}$ and *Parp1*$^{+/-}$ mice. (*G* and *H*) Standard triplex genotyping PCR (*G*) and Targeted AN-specific PCR (*H*) of tail DNA from 7 to 10-d old F1 *Parp1*$^{+/A}$ chimera mice and controls. ID number 1 to 3 identifies unique pups. The lower band of the doublet in panel *G* represents a hybrid between the A and WT allele PCR products due to their share 230-bp sequence. This band only appears in PCR from *Parp1*$^{+/A}$ mice when both the WT and the A alleles are present. (*I*) qPCR of *Parp1*^{AN} in peripheral blood of F1 *Parp1*$^{+/A}$ mice of different ages.

PARP1-E988A foci is likely caused by continuous recruitment of different PARP1-E988A proteins to the unrepaired breaks. This is similar to what we and others have reported for clinical PARPi-treated PARP1-WT (11). Thus, these data suggest that inactive PARP1 (E988A) can occupy the DNA breaks for an extended time, where it blocks other repair proteins from accessing the ends.

Isolated *Parp1*$^{+/A}$ Cells Support Significant DNA Damage-Induced PARylation. Next, we isolated *Parp1*$^{+/A}$ and *Parp1*$^{-/-}$ SV40 antigens immortalized murine embryonic fibroblasts (iMEFs) and confirmed by genotyping (*SI Appendix*, Fig. S2 *C* and *D* and Table S1) to understand how inactive Parp1 dominant negatively blocks embryonic development. We also validated that the A allele is expressed in the *Parp1*$^{+/A}$ iMEF cells via RT-PCR. The nucleotides encoding Glutamine 988 reside at the junction between Exon 22 and 23 (*SI Appendix*, Fig. S2*E*). The targeting created a new MluI digestion site in the cDNA (but not in genomic DNA). MluI digestion of RT-PCR products derived from *Parp1*$^{+/A}$ cells detected two bands of equal intensities, indicating the A allele is expressed at levels comparable to the WT allele (*SI Appendix*, Fig. S2*E*). Correspondingly, sequencing of the cDNA derived from *Parp1*$^{+/A}$

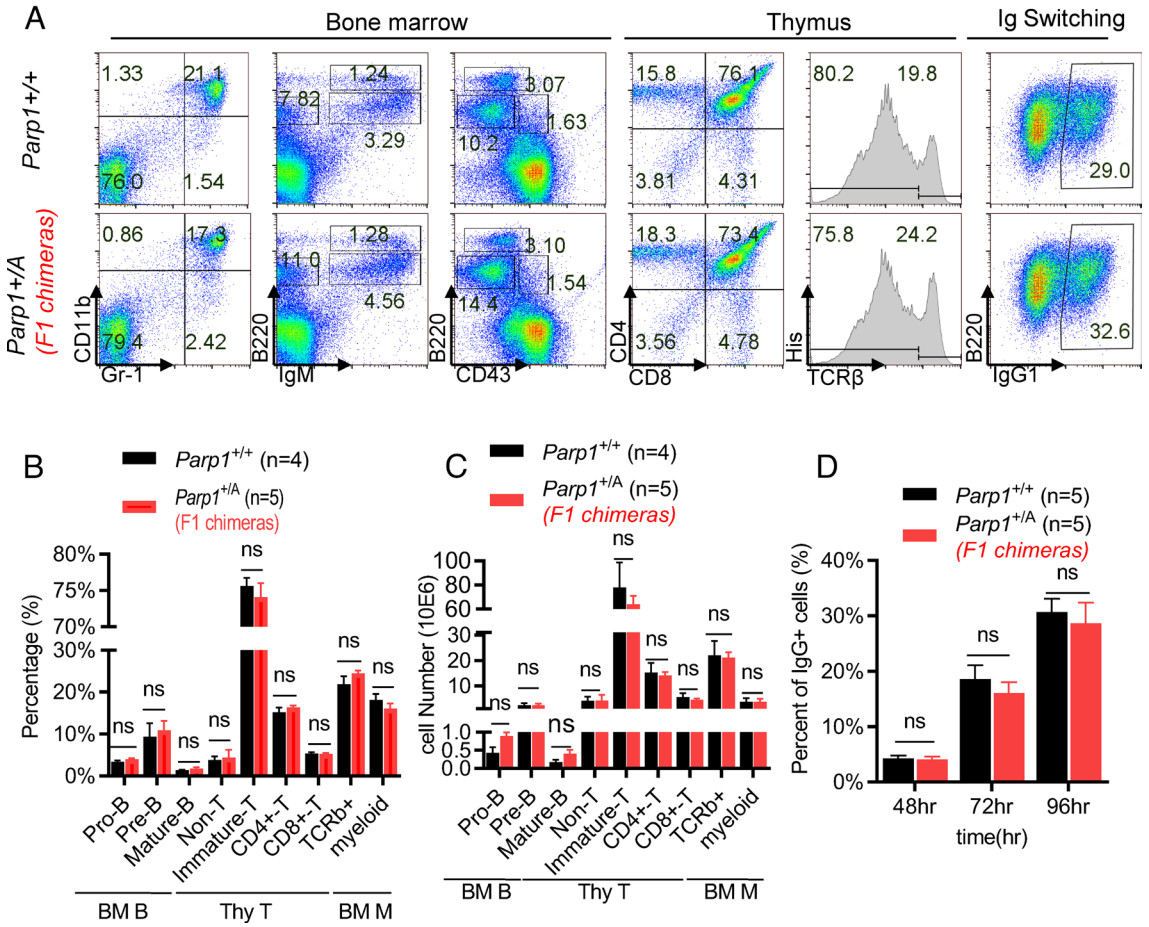

Fig. 3. Young F1 chimeric *Parp1*$^{+/A}$ mice have normal lymphocyte development. (*A*–*D*) Representative flow cytometry analyses (*A*), relative percentage (*B*), and absolute cell count (*C*) of *Parp1*$^{+/A}$ mice lymphocyte and myeloid development, as well as naïve B lymphocytes CSR efficiency (*D*). The Student's *t* test was applied to calculate the *P* value. ns: $P > 0.05$.

cells also revealed mixed cDNA at the A->C mutation (leading to Glu to Ala) and silent mutation T->C (Asn-> Asn) (*SI Appendix*, Fig. S2*F*). Together these data confirmed that the Parp1^{A} allele is expressed at a comparable level to the WT allele in the *Parp1*$^{+/A}$ iMEFs.

In previous studies, we showed that the majority of PARP2 is recruited to DNA damage sites by the PAR chain generated by PARP1 and that the presence of PARP1 protein prevents DNA-dependent recruitment and activation of PARP2 (26). Given loss of both PARP1 and PARP2 led to embryonic lethality, we hypothesized that the presence of inactive PARP1 might simply abolish the PARylation by both PARP1 and PARP2 by blocking the remaining PARP1 and PARP2 activation. To test this, we first measured PARylation-dependent recruitment of XRCC1 to DNA damage foci in *Parp1*$^{+/A}$ cells. The intensity of the RFP-XRCC1 foci in *Parp1*$^{+/A}$ iMEFs was higher than *Parp1*$^{-/-}$ iMEFs while also lower than *Parp1*$^{+/+}$ iMEFs (Fig. 5*A*). Next, we measured pan-ADP-ribosylation using western blot. The ADP-ribose has a molecular weight of 559.3157g/mol (=0.559 KDa). Thus, MARylation or adding a few ADP-Ribose units cannot cause measurable molecular weight shifts on western blotting. The major molecular weight shift in Fig. 5*B* results from extensive PARylation. Both baseline and damage-induced auto-ADP-ribosylation of PARP1 and histones are comparable in *Parp1*$^{+/A}$ and control *Parp1*$^{+/+}$ iMEFs and significantly higher than that of *Parp1*$^{-/-}$ iMEFs (Fig. 5 *B* and *C*). This is consistent with the notion that the E988A mutation preserves some mono-ADP-ribosylation (MARylation) activity (11) and the inactive PARP1 (E988A) does not abrogate the activation of the WT PARP1 in the *Parp1*$^{+/A}$ cells. In this context, we have shown that E988A PARP1, like WT PARP1, can exchange at the site of damage efficiently (Fig. 4*F*), which explains why E988A did not prevent WT PARP1 from being activated by DNA breaks. Consistent with Parp1 (regardless of activity) blocking PARP2 activation, Parp2 auto-ADP-ribosylation is highest in *Parp1*$^{-/-}$ cells, and lower in both *Parp1*$^{+/+}$ and *Parp1*$^{+/A}$ cells. Next, we used an antibody specific for PARylation (cannot detect MARylation). We found that H_2O_2-induced auto-PARylation in *Parp1*$^{+/A}$ cells is comparable with that of *Parp1*$^{+/-}$ iMEFs, and much higher than that of *Parp1*$^{-/-}$ iMEFs (Fig. 5*D*). This result is consistent with the intramolecular auto-PARylation mode of PARP1. In both *Parp1*$^{+/A}$ and *Parp1*$^{+/-}$ iMEFs only one copy of the PARP1 can be auto-PARylated. Collectively, the result suggests that the embryonic lethality of *Parp1*$^{+/A}$ mice cannot be explained by the lack of overall ADP-ribosylation or PARylation. Instead, the continuous recruitment and the presence of inactive Parp1 protein at DNA damage lesions might physically block DNA repair by preventing other proteins (e.g., PARP2) from accessing the ends.

Inactivated PARP1 Protein Selectively Blocks Single-Strand Breaks Repair and Topo-II Lesions. DNA strand breaks, both single- and DSBs, recruit and activate PARP1. To understand the types of DNA repair events blocked by *Parp1*^{A}, we isolated *Parp1*$^{+/A}$ and *Parp1*$^{-/-}$ embryonic stem (ES) cells and confirmed via PCR that they do not have the *Parp1*^{AN} allele (*SI Appendix*, Fig. S2 *C* and *D*). ES cells were chosen because their inherent checkpoint

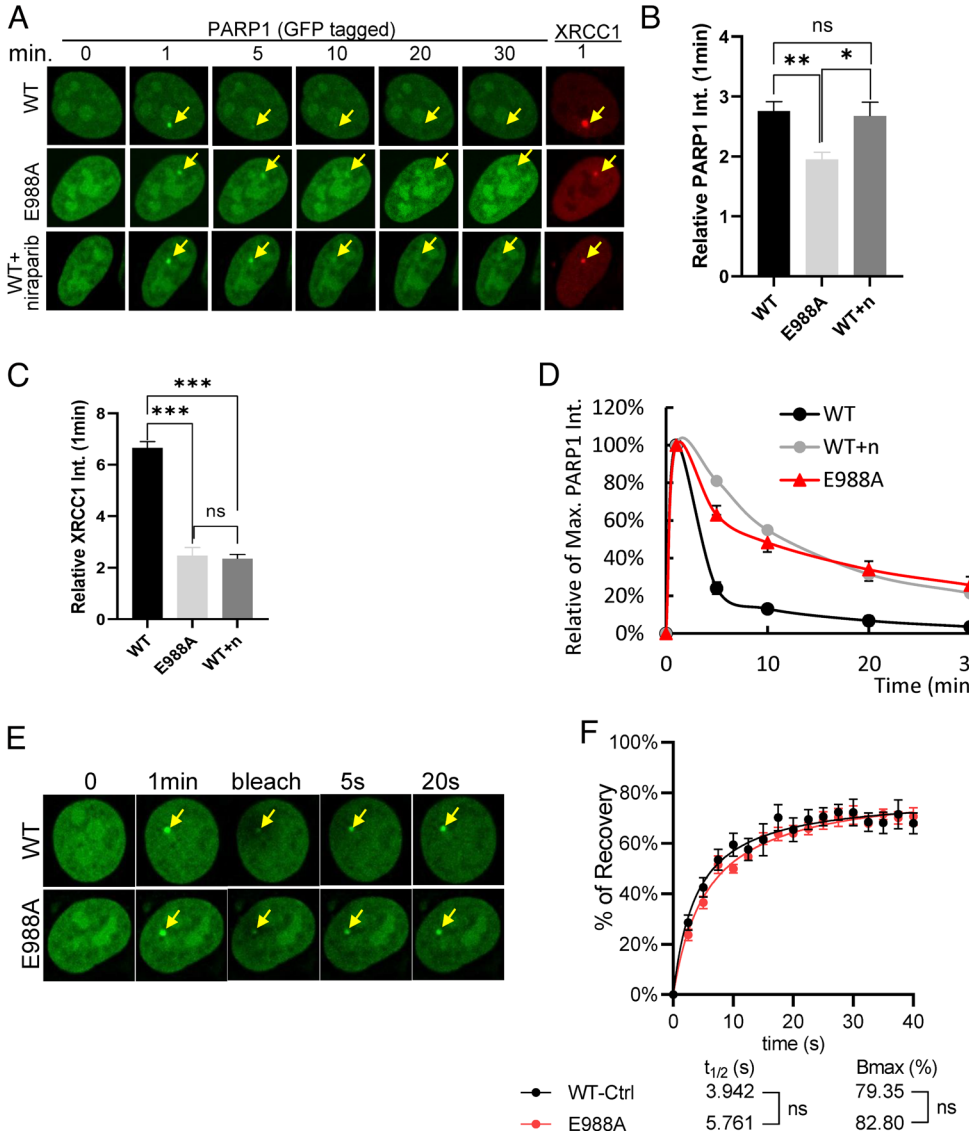

Fig. 4. Inactive Parp1 forms persistent DNA damage-induced foci without exchange defects. Summary of quantitative live-cell imaging following laser microirradiation in the PARP1 knockout U2OS cells. The time (minutes) in this figure indicates the time after 405-nm laser-induced microirradiation. (*A*) Representative images of GFP-tagged PARP1(in green) and RFP-tagged XRCC1 (in red) after microirradiation. Niraparib (1 μM) was added 1 h before the microirradiation. (*B*) Quantification of relative PARP1 foci intensity (as a ratio of GFP intensity at the foci vs. nuclear average) at 1 min after microirradiation. (*C*) Quantification of relative XRCC1 foci intensity at 1 min after microirradiation. (*D*) The normalized kinetics (as a percentage of the maximal relative intensity) of GFP-tagged E988A-PARP1 or wild-type PARP1 in PARP1-deficient U2OS cells with or without 1 μM niraparib after laser microirradiation. ns: $P > 0.05$, *$P < 0.05$, **$P < 0.01$, and ***$P < 0.001$. (*E* and *F*) Representative FRAP images (*E*) and recovery curves (*F*) of E988A-PARP1 and wild-type PARP1. The foci area was bleached by 488-nm laser at 1 min after microirradiation.

defects would allow us to visualize chromosomal instability in metaphase preparations easily. Mitotic bridge formation was increased in both *Parp1*$^{+/A}$ and *Parp1*$^{-/-}$ ES cells to similar levels (Fig. 5*E*). Meanwhile, in comparison to the *Parp1*$^{+/+}$ ES cells, the frequency of sister-chromatid exchanges (SCEs) per chromosome increased ~2.4 fold in *Parp1*$^{-/-}$ ES cells, and ~5.5-fold in *Parp1*$^{+/A}$ ES cells (Fig. 5*F*). Despite the genomic instability, *Parp1*$^{+/A}$ and *Parp1*$^{-/-}$ iMEFs proliferated at similar levels as the matched *Parp1*$^{+/+}$ control (5) (Fig. 6*A*).

Using this genotype and expression validated *Parp1*$^{+/A}$ iMEF, we measured HR and NHEJ (and microhomology mediated end-joining -MMEJ) using the DR-GFP and EJ5 reporters, respectively. After the reporter has been integrated into the *Parp1*$^{+/A}$ and control iMEF, transient expression of I-SceI induces GFP conversion via HR in DR-GFP reporter containing cells (27) and via NHEJ, and to a lesser extent MMEJ, in EJ5 containing cells (28). Consistent with normal meiosis in the young *Parp1*$^{+/A}$ F1 chimeras, *Parp1*$^{+/A}$ and *Parp1*$^{-/-}$ iMEFs support DR-GFP conversion at levels comparable to or even higher than the *Parp1*$^{+/+}$ iMEFs (Fig. 6*B*). ATM inhibitor treatment significantly reduced DR-GFP conversion in *Parp1*$^{+/+}$ cells, serving as a control (Fig. 6*B*) (29–31). In parallel, EJ5 conversion is also very efficient in *Parp1*$^{+/A}$ and *Parp1*$^{-/-}$ iMEFs (Fig. 6*C*). The elevated levels of DR-GFP in *Parp1*$^{+/A}$ and *Parp1*$^{-/-}$ iMEFs are not due to high copies of the substrates in *Parp1*$^{+/A}$ and *Parp1*$^{-/-}$ iMEFs (*SI Appendix*, Fig. S3 *A* and *B*) but might reflect the increased SCE in *Parp1*$^{+/A}$ and *Parp1*$^{-/-}$ cells (Fig. 5*F*). Together with the normal lymphocyte development and meiosis in the young F1 *Parp1*$^{+/A}$ mice, the results suggest that inactive PARP1 did not abrogate HR or NHEJ.

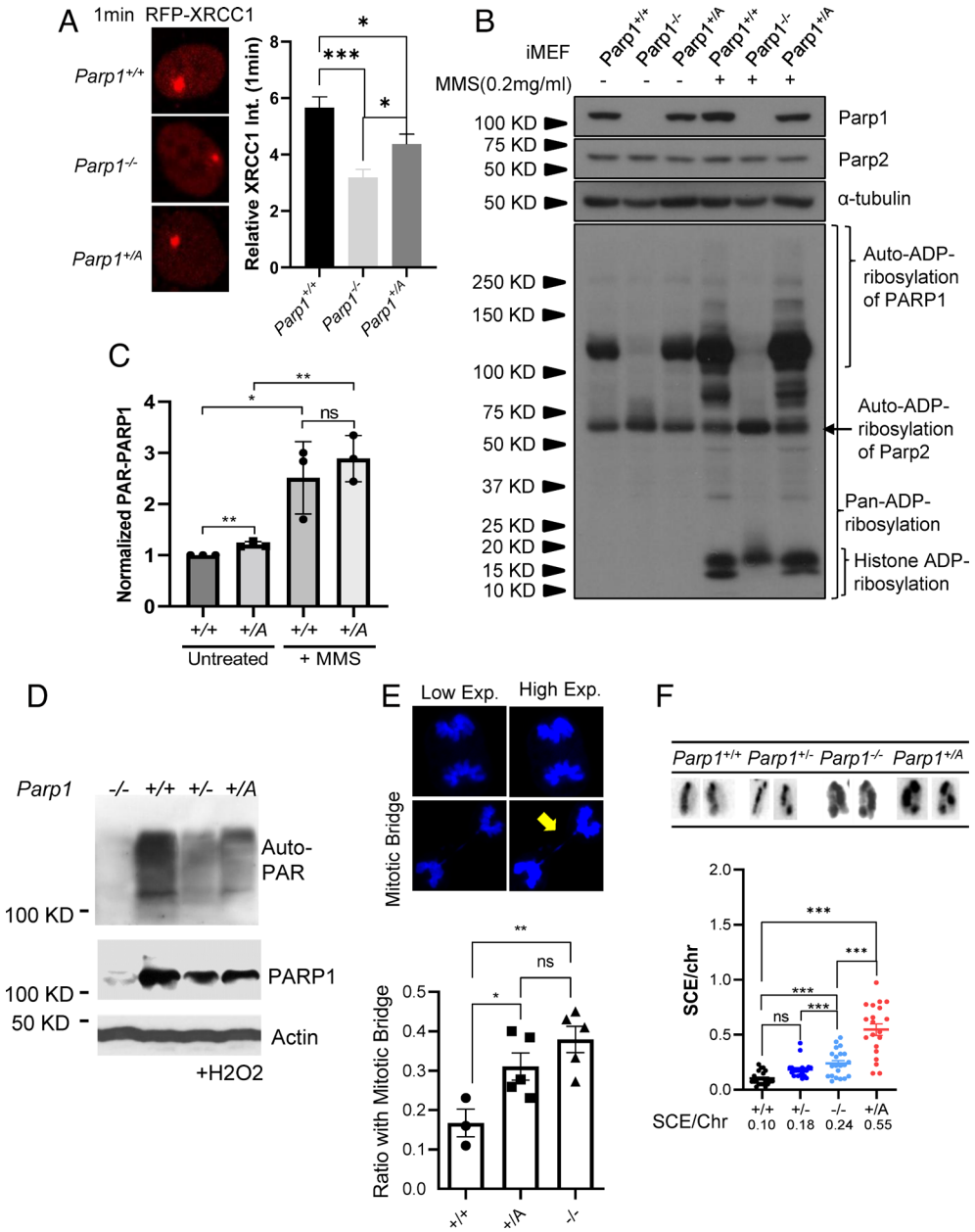

Fig. 5. PARP1 E988A causes increased SCE in a dominant-negative manner without ablating DNA damage-induced PARylation in *Parp1*$^{+/A}$ cells. (*A*) Representative images and 1-min intensity of RFP tagged XRCC1 foci in *Parp1*$^{+/+}$, *Parp1*$^{-/-}$, and *Parp1*$^{+/A}$ immortalized MEFs after 405-nm laser microirradiation. (*B* and *C*) Representative western blot (*B*) and quantification of pan-AND-ribosylated PARP1 and PARP2 in *Parp1*$^{+/+}$, *Parp1*$^{-/-}$, and *Parp1*$^{+/A}$ immortalized MEFs after 0.2 mg/mL of MMS treatment (*C*). *$P < 0.05$ and **$P < 0.01$, *P*-value was calculated by Student's *t* test. (*D*) Western blot of PAR in H_2O_2 stimulated *Parp1*$^{-/-}$, *Parp1*$^{+/+}$, *Parp1*$^{+/-}$, and *Parp1*$^{+/A}$ immortalized MEFs. (*E*) Representative images showing normal mitotic cells (*Top*) or cells with a mitotic bridge (*Bottom*) and frequency of mitotic bridges in *Parp1*$^{+/+}$, *Parp1*$^{-/-}$, and *Parp1*$^{+/A}$ immortalized MEFs. (*F*) Representative images and statistics of SCE rate of *Parp1*$^{+/+}$, *Parp1*$^{+/-}$, *Parp1*$^{-/-}$, and *Parp1*$^{+/A}$ ES cells. The *P* value was calculated based on one-way ANOVA. ***$P < 0.001$.

To understand what other type of DNA repair was blocked by inactive PARP1, we measured DNA damage sensitivity using *Parp1*$^{+/A}$ and control iMEFs. Even in comparison to *Parp1*$^{-/-}$ iMEFs, *Parp1*$^{+/A}$ iMEFs were much more sensitive to the alkylating agent methyl-methanesulfonate (MMS) (Fig. 6*D* and *SI Appendix*, Fig. S3*C*), the Topoisomerase I inhibitor camptothecin (CPT) (Fig. 6*E* and *SI Appendix*, Fig. S3*D*) and, perhaps unexpectedly, the Topoisomerase II inhibitor etoposide (Fig. 6*F*). *Parp1*$^{-/-}$ cells are also sensitive to MMS and CPT, albeit less than their *Parp1*$^{+/A}$ counterpart, consistent with a role of PAR and PAR-mediated recruitment of XRCC1 in BER and Top1-poison removal (Fig. 6 *D* and *E*). In this context, XRCC1 deficiency has also been linked with MMS and CPT hypersensitivity (2). But etoposide sensitivity has not been reported in XRCC1-deficient cells. The hypersensitivity of *Parp1*$^{+/A}$ cells to Topo-II block and the normal lymphocyte development and spermatogenesis in young F1 *Parp1*$^{+/A}$ chimera mice, together with their HR and NHEJ/MMEJ proficiency measured by the DR-GFP and EJ5 reporters (Fig. 6 *B* and *C*), suggest inactive PARP1, but not lack of PARP1, might block the processing of end-blocked lesions, especially during replication, likely independent of NHEJ or HR. Consistent with this notion, *Parp1*$^{+/A}$ and *Parp1*$^{-/-}$ iMEF displayed relatively consistent and comparable levels of hypersensitivity to radiation (Fig.6*G* and *SI Appendix*, Fig. S3*E*).

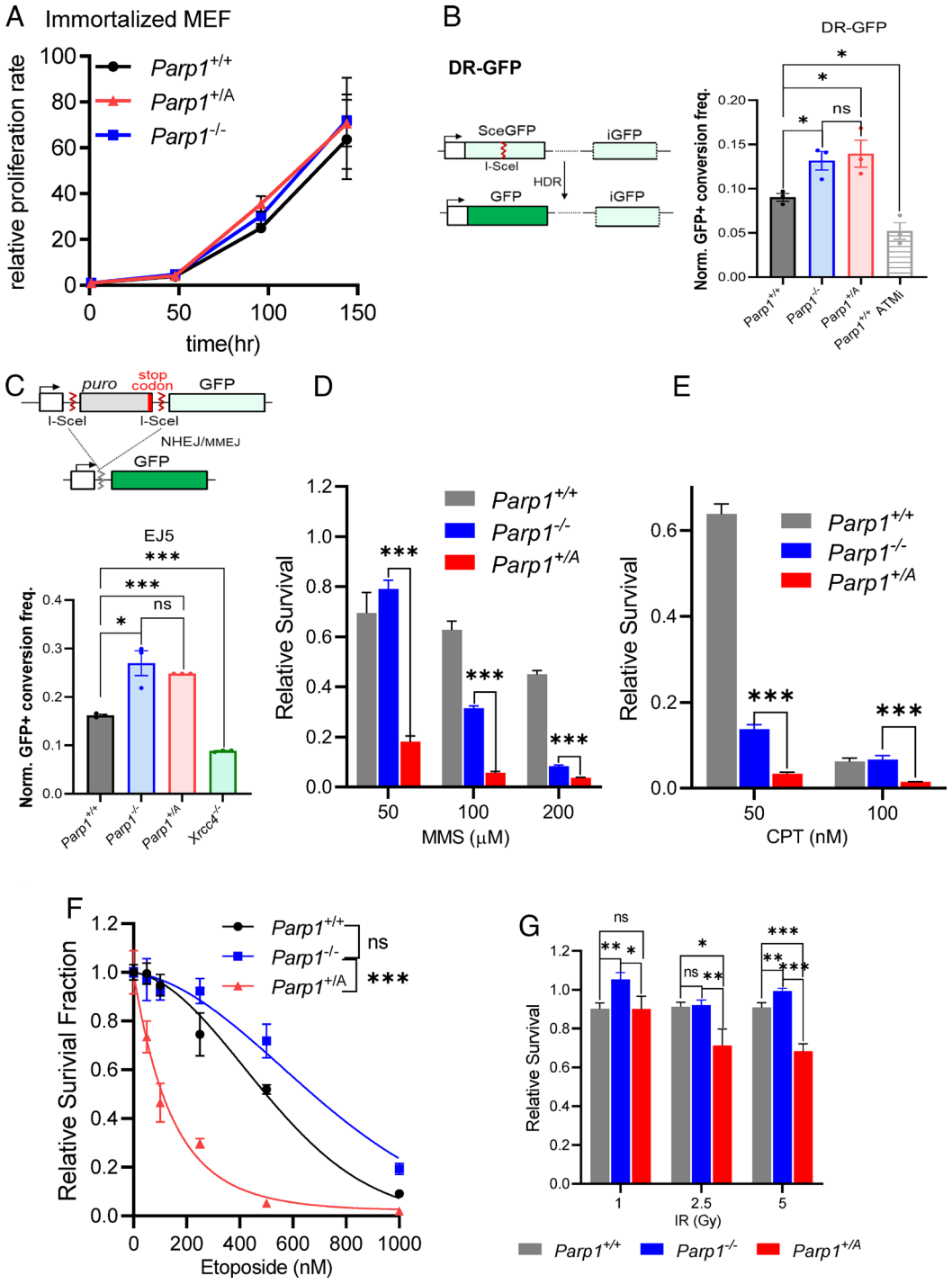

Fig. 6. PARP1 E988A dominant negatively inhibits selective DNA repair pathways without ablating HR or NHEJ repair. (*A*) The proliferation rate of *Parp1*$^{+/+}$, *Parp1*$^{-/-}$, *and Parp1*$^{+/A}$ immortalized MEFs. (*B*) Sketch diagram and HR efficiency measured by the frequency of GFP+ cells in *Parp1*$^{+/+}$, *Parp1*$^{-/-}$, and *Parp1*$^{+/A}$ immortalized MEFs with *Parp1*$^{+/+}$ + ATMi (KU-55933 15 μM, Selleckhem, S1092) control using DR-GFP reporter. Student's *t* test was used to calculated *P*-value, ns: $P > 0.05$ and $^{*}P < 0.05$. (*C*) Sketch diagram and NHEJ efficiency measured by the frequency of GFP+ cells in *Parp1*$^{+/+}$, *Parp1*$^{-/-}$, and *Parp1*$^{+/A}$ immortalized MEFs with *Xrcc4*$^{-/-}$ immortalized MEFs control using EJ5 reporter. *P*-value was calculated by Student's *t* test, ns: $P > 0.05$, $^{*}P < 0.05$, and $^{***}P < 0.001$. (*D*–*G*) Sensitivity of *Parp1*$^{+/+}$, *Parp1*$^{-/-}$, and *Parp1*$^{+/A}$ immortalized MEFs to MMS (*D*), CPT (*E*), etoposide (*F*), and IR (*G*). The *P*-value was calculated via Student's *t* test and extra sum-of-square F test using the dose–response model. All dots and error bars represent means and SEs. ns: $P > 0.05$, $^{*}P < 0.05$, $^{**}P < 0.01$, and $^{***}P < 0.001$.

Discussion

Taken together, the early embryonic lethality of *Parp1*$^{+/A}$ mice provides strong evidence for substantial toxicity of catalytically inactive PARP1 protein in otherwise normal tissues. This is in sharp contrast to the normal development of *Parp1*$^{-/-}$ mice. In this context, *Parp1*$^{+/A}$ cells share many features with PARPi-treated normal cells (18) and XRCC1-deficient cells (2, 3), including BER deficiency, increased SCE, and persistent PARP1 foci without allosteric locking (11, 14). Conversely, unlike the PARPi-treated cells, the overall ADP-ribosylation activity in the *Parp1*$^{+/A}$ cells closely resembles the *Parp1*$^{+/+}$ cells, and is much higher than in *Parp1*$^{-/-}$ cells (Fig. 5 *B* and *C*). The damage-induced auto-PARylation of PARP1 in *Parp1*$^{+/A}$ cells is similar to *Parp1*$^{+/-}$ cells (Fig. 5*D*), consistent with both lines having only one copy of active PARP1 that can auto-PARylate itself. Loss of PARP1 leads

to resistance to PARP inhibitors (11, 32). Together these data support a model in which the presence of inactive PARP1, but not the lack of PARP1-mediated PARylation in general, underlies the normal tissue toxicity of PARP inhibition. Moreover, it suggests that if half of the PARP1 is inactive, it is sufficient to cause major normal tissue toxicity. Given the development impairment of *Parp1*$^{+/A}$ cells even without small molecule inhibitors, and the efficient exchange of PARP1-E988A at the microirradiation sites, our results also suggest that the small molecule induced reverse-allosteric locking of PARP1, although may be important for inhibitor function, are not essential for normal tissue toxicity. It is the presence of inactive PARP1 with high-affinity DNA binding that is toxic. In this context, the kinetics of PARylation, thus enzymatic activity might be important for preventing persistent PARP1 foci (33). HPF1 was recently identified as an essential modulator for PARP1 activity on Serine (34). Lack of HPF1 and similar modulators also causes persistent PARP1 foci and toxicity, offering additional strategies for targeting PARP1.

How does the inactive PARP1 differ from PARP1 deletion? MMS-induced PARP2 auto-ADP-ribosylation increased in *Parp1*$^{-/-}$ cells, but not in *Parp1*$^{+/A}$ cells (Fig. 5 *B* and *C*), suggesting the presence of inactive Parp1 blocks PARP2 activation and automodification. It is possible PARP2 is only one of the many repair proteins that is blocked by inactive PARP1. As a result, while both *Parp1*$^{+/A}$ cells and *Parp1*$^{-/-}$ cells are hypersensitive to MMS and Topo I inhibitors, the hypersensitivity to Topo II inhibitors seems unique to the presence of inactive PARP1 and has not been found with PARP1 or XRCC1 deletion (2, 3). Among the genotoxic anticancer therapies, alkylating agents and Topo II inhibitors carry a particularly high risk for therapy-induced MDS/AML (t-MDS/AML) and clonal hematopoiesis. Thus, the hypersensitivity of *Parp1*$^{+/A}$ cells to these agents might explain the severe hematological toxicity and t-MDS/AML associated with PARP inhibitors (17, 19), a hypothesis that can be tested by somatic inactivation models.

The *Parp1*$^{+/A}$ mouse model described here provides strong evidence for severe toxicity of the inactive PARP1 protein during embryonic development in vivo. PARP1 resembles the ATM, ATR, and DNA-PK kinases, which also exhibit more severe phenotypes when enzymatically impaired than when deleted entirely (35). They all share a common feature. All are recruited to and activated at the site of DNA damage. The activation is coupled with a rapid exchange of the proteins at the DNA damage site. The presence of the inactive protein not only blocks the further activation of the signaling cascade, but also occupies the DNA lesion, where it blocks the activation of other sensors or DNA repair itself. This model is consistent with the fact that no "inactivation" mechanism for these DNA damage response factors exists. These insights should guide the development of therapeutic agents that circumvent the normal tissue toxicities associated with current PARP1, ATM, and ATR inhibitors.

Materials and Methods

Mice. The 5′ and 3′ arms of the Parp1^{E988A} targeting construct were amplified from 129/sv mouse ES cells' genomic DNA, mutated in exon22 encoding E988A, and cloned into the pEMC-neo targeting vector with a PGK-neo-resistance (neo-R) cassette flanked by FRTs. Targeted ES clones were screened by PCR first and confirmed via Southern blotting (HindIII and KpnI digestion with both 5′ and 3′ probes) (Fig. 1*B* and *SI Appendix*, Table S1). The successfully targeted ES clones were injected for germline transmission. The *Parp1*$^{+/AN}$ chimeras with the neo-R cassette were bred with Rosa26a$^{FLIP/FLIP}$ (Jax Strain No. 003946 in 129Sv) mice to generate the F1 *Parp1*$^{+/A}$ mice. The presence of the NeoR in Parp1^{AN} allele interferes with the expression of Parp1, resulting in no or little Parp1 expression. The *P*-value of birth rates was calculated using χ^2 test. Genotypings were carried out by PCR with 230-bp product for *Parp1*$^{+}$, 315 bp for *Parp1*^{A}, and440 bp for *Parp1*^{AN} in the triplex PCR, and 340 bp for only AN (Fig. 2 *G* and *H* and *SI Appendix*, Figs. S1 *C* and *D* and S2 *C* and *D* and Table S1). All animal work was carried out with the guidelines established by the Institutional Animal Care and Use Committee at Columbia University Medical Center.

Western Blot Antibodies. Primary antibodies used in this study for western blot include: anti-PARP1 antibody (Cell Signaling Technology, 9542, 1:2,000), anti-PARP2 antibody (Active Motif, 39044, 1:2,000), anti-α-Tubulin antibody (Sigma, CP06, 1:1,000), anti-pan-ADP-ribose binding reagent (Sigma, MABE1016, 1:1,000), anti-β-actin (Sigma, A5441, 1:10,000), and anti-PAR antibody (R&D, 4335-MC-100, 1:1,000).

Mouse Hematopoietic Cell and Lymphocyte Analyses. Mouse blood cell and lymphocyte development were analyzed by flow cytometry (36, 37). B lymphocyte development was conducted by staining with cocktails including FITC anti-mouse CD43 (Biolegend, 553270), PE goat anti-mouse IgM (Southern Biotech, 1020-09), PE-cyanine5 anti-Hu/Mo CD45R (B220) (eBioScience, 15-0452-83), and APC anti-mouse TER119 (Biolegend, 116212). T lymphocyte development was measured on thymocytes using cocktail including PE rat anti-mouse CD4 (BD Pharmingen, 557308), FITC anti-mouse CD8a (Biolegend, 100706), PE/Cy5 anti-mouse CD3e (eBioscience, 15-0031-83), and APC anti-mouse TCRβ (BD Pharmingen, 553174). Myeloid cells were measured in bone marrow cells and splenocytes using cocktail including FITC anti-mouse CD11b (BD Pharmingen, 553310), PE rat anti-mouse CD19 (BD Pharmingen, 557399), PE/Cy5 anti-mouse CD3e (eBioscience, 15-0031-83), and APC anti-mouse Ly6G/Ly6C(Gr-1) (Biolegend, 108412). Purified splenocyte CSR was stained with PE-cyanine5 anti-Hu/Mo CD45R (B220) and FITC rat anti-mouse IgG1(BD Pharmingen, 553443). All antibodies were diluted according to the manufacturer's protocol. The flow cytometry data were collected on either an LSR II (BD), or on an Attune NxT (Invitrogen) flow cytometer. All flow cytometry data were analyzed using FlowJo V10.

Cell Line Derivation and Sensitivity Assay. The *Parp1*$^{+/+}$, *Parp1*$^{-/-}$, *Parp1*$^{+/-}$, and F1 *Parp1*$^{+/A}$ MEFs were derived from E13.5 to E14.5 embryos and functionally and genotyping verified (*SI Appendix*, Fig. S2 *C* and *D*). The *Parp1*$^{+/+}$, *Parp1*$^{-/-}$, *Parp1*$^{+/-}$ and *Parp1*$^{+/A}$ ES cells were derived at the HICCC transgenic mouse core facility and cultured on irradiated (30 Gy) fibroblast feeders as detailed before (38, 39). For the survival assay, ~1,000 cells/well were plated into a 96-well plate. Cells were irradiated by ionizing radiation (IR, 1, 2.5, or 5 Gy) 24 h after plating. Genotoxins were added 24 h after initial plating at the concentration indicated in the figures–camptothecin (CPT, Sigma, 208925) 50, and 100 nM; etoposide (Sigma, E1383) 50, 100, 250, 500, and 1,000 nM; and MMS (Sigma, 129925) 50, 100, and 200 μM. The CyQUANT™ Cell Proliferation Assay kit (Invitrogen, C7026) was used to measure cell numbers after 7 d. The survival curves were generated with GraphPad Prism V8.0 using the nonlinear regression linear quadratic cell death model, and *P*-value was calculated based on coefficient of killing.

Adult Male Mouse Epididymal Sperm Count and Sperm DNA Preparation. Mice sperm counts and histology analyses of the adult testis (<8 wk) were carried out as detailed before (40). Testes were fixed in Bouin's fixative (ICCA, 1120-16) for Periodic Acid Schiff staining. Cauda epididymis was minced in PBS and incubated at 32 °C for 20 min to let all sperms swim out. Sperm suspension was filtered through a 70-μm nylon cell strainer and counted under a microscope using a hematocytometer. Sperm mobility was determined as: grade a: immotile, b: nonprogressive, c: slow progressive, or d: rapid progressive.

Live-Cell Imaging. Live-cell imaging and FRAP were conducted as previously described with minor revisions (10, 11). Plasmids encoding GFP-tagged WT or E988A PARP1, together with RFP-tagged XRCC1 (a generous gift from Dr. Li Lan at MGH), were transfected into PARP1 knockout U2OS cells (11) using Lipofectamine 2000 (Invitrogen, 11668019). Live-cell images were acquired via the NIS Element High Content Analysis software (Nikon Inc.) at different times after damage (inflicted by 405-nm laser without priming) and every 2.5 s after photobleaching (via a 488-nm laser) at 1 min after initial damage for FRAP. *P*-values of exchange curves were calculated based on extra sum-of-square F test using the dose–response model. All Dots and error bars represent means and SEs. All images' analyses were carried out with Fiji ImageJ software.

HR and NHEJ Reporter Assay. The DR-GFP, EJ5, and I-SceI plasmids were generous gifts from Dr. Jeremy Stark at the City of Hope, and the assays were carried out as previously detailed (28) with minor modifications. Briefly, the DR-GFP plasmid contains an upstream SceGFP cassette in which the GFP expression was interrupted by an I-SceI recognition site, and a downstream GFP template truncated at both termini. After I-SceI induced DSB, a successful HR repair using the downstream iGFP as template would convert the SceGFP cassette into an expressing GFP cassette. The EJ5 plasmid consists of a GFP cassette downstream of a puromycin ORF flanked by two I-SceI sites following a single promoter, in which the stop codon in the puromycin ORF prevents GFP expression. Successful NHEJ repair following I-SceI digestion restores GFP expression. Both the DR-GFP and EJ5 plasmids were linearized and electroporated (BioRad Gene Pulser Xcell™ system, 800 V, 10 μF, 300 Ω, 0.4-cm cuvettes) into immortalized *Parp1*$^{+/+}$, *Parp1*$^{-/-}$, F1 *Parp1*$^{+/A}$, and *Xrcc4*$^{-/-}$ MEFs separately. After 6 d of puromycin selection and expansion, I-SceI plasmid was transiently transfected into the stable cell lines using lipofectamine 2000 following the manufacturer's protocol. Frequency of GFP expressing cells was measured by flow cytometry at D3 after I-SceI transfection, and HR and NHEJ efficiency was calculated by normalizing GFP+ population to the efficiency of GFP expressing vector transfection control to elucidate the effect of transfection efficiency. All reporter assays were repeated for additional 2 times, and all flow cytometry data were analyzed using FlowJo V10.

Data, Materials, and Software Availability. There are no data underlying this work.

ACKNOWLEDGMENTS. We thank Dr. Chyuan-Sheng (Victor) Lin for helping with germline injection, Dr. Theresa Swayne for helping with confocal analyses, and Dr. Jeremy Stark for his great help and discussion about the DR-GFP and EJ5 reporter assays. This work was partly supported by NIH R01 CA226852, CA271595, CA275184 to S.Z., HD085904 to M.M.S., and 1P01CA174653 to S.Z. and R.B. S.Z. was a scholar of the Leukemia & Lymphoma Society. This research used flow cytometry, molecular cytogenetic, transgenic, and confocal and specialized microscopy shared resources funded through the NIH/NCI Cancer Center Support Grant P30CA013696 to the HICCC of Columbia University.

Author affiliations: [a]Institute for Cancer Genetics, Vagelos College of Physicians and Surgeons, Columbia University, New York City, NY 10032; [b]Department of Medicine, Columbia University Medical Center, New York, NY 10032; [c]Department of Genetics and Development, Columbia University Medical Center, New York, NY 10032; [d]Department of Urology, Columbia University Medical Center, New York, NY 10032; [e]Department of Systems Biology, Columbia University Medical Center, New York, NY 10032; [f]Department of Pathology and Cell Biology, Vagelos College of Physicians and Surgeons, Columbia University, New York City, NY 10032; [g]Department of Immunology and Microbiology, Vagelos College of Physicians and Surgeons, Columbia University, New York City, NY 10032; and [h]Division of Pediatric Oncology, Hematology and Stem Cell Transplantation, Department of Pediatrics, Vagelos College of Physicians and Surgeons, Columbia University, New York City, NY 10032

1. S. S. David, V. L. O'Shea, S. Kundu, Base-excision repair of oxidative DNA damage. *Nature* **447**, 941–950 (2007).
2. K. W. Caldecott, XRCC1 protein; Form and function. *DNA Repair (Amst)* **81**, 102664 (2019).
3. K. W. Caldecott, DNA single-strand break repair and human genetic disease. *Trends Cell Biol.* **32**, 733–745 (2022), 10.1016/j.tcb.2022.04.010.
4. K. Azarm, S. Smith, Nuclear PARPs and genome integrity. *Genes Dev.* **34**, 285–301 (2020).
5. Z. Q. Wang *et al.*, PARP is important for genomic stability but dispensable in apoptosis. *Genes Dev.* **11**, 2347–2358 (1997).
6. H. Farmer *et al.*, Targeting the DNA repair defect in BRCA mutant cells as a therapeutic strategy. *Nature* **434**, 917–921 (2005).
7. H. E. Bryant *et al.*, Specific killing of BRCA2-deficient tumours with inhibitors of poly(ADP-ribose) polymerase. *Nature* **434**, 913–917 (2005).
8. J. Murai *et al.*, Stereospecific PARP trapping by BMN 673 and comparison with olaparib and rucaparib. *Mol. Cancer Ther.* **13**, 433–443 (2014).
9. J. Murai *et al.*, Trapping of PARP1 and PARP2 by clinical PARP inhibitors. *Cancer Res.* **72**, 5588–5599 (2012).
10. X. Lin *et al.*, PARP inhibitors trap PARP2 and alter the mode of recruitment of PARP2 at DNA damage sites. *Nucleic Acids Res.* **50**, 3958–3973 (2022).
11. Z. Shao *et al.*, Clinical PARP inhibitors do not abrogate PARP1 exchange at DNA damage sites in vivo. *Nucleic Acids Res.* **48**, 9694–9709 (2020).
12. J. Rudolph, K. Jung, K. Luger, Inhibitors of PARP: Number crunching and structure gazing. *Proc. Natl. Acad. Sci. U.S.A.* **119**, e2121979119 (2022).
13. M. F. Langelier, L. Zandarashvili, P. M. Aguiar, B. E. Black, J. M. Pascal, NAD(+) analog reveals PARP-1 substrate-blocking mechanism and allosteric communication from catalytic center to DNA-binding domains *Nat. Commun.* **9**, 844 (2018).
14. L. Zandarashvili *et al.*, Structural basis for allosteric PARP-1 retention on DNA breaks. *Science* **368**, eaax6367 (2020).
15. J. Rudolph, J. Mahadevan, P. Dyer, K. Luger, Poly(ADP-ribose) polymerase 1 searches DNA via a "monkey bar" mechanism. *Elife* **7**, e37818 (2018).
16. J. Rudolph *et al.*, The BRCT domain of PARP1 binds intact DNA and mediates intrastrand transfer. *Mol. Cell* **81**, 4994–5006.e5 (2021).
17. P. G. Pilie, A. George, T. A. Yap, Patient selection biomarker strategies for PARP inhibitor therapy. *Ann. Oncol.* **31**, 1603–1605 (2020).
18. S. Ito, C. G. Murphy, E. Doubrovina, M. Jasin, M. E. Moynahan, PARP inhibitors in clinical use induce genomic instability in normal human cells. *PLoS One* **11**, e0159341 (2016).
19. C. J. LaFargue, G. Z. Dal Molin, A. K. Sood, R. L. Coleman, Exploring and comparing adverse events between PARP inhibitors. *Lancet Oncol.* **20**, e15–e28 (2019).
20. A. L. Winship *et al.*, The PARP inhibitor, olaparib, depletes the ovarian reserve in mice: Implications for fertility preservation. *Hum. Reprod.* **35**, 1864–1874 (2020).
21. G. T. Marsischky, B. A. Wilson, R. J. Collier, Role of glutamic acid 988 of human poly-ADP-ribose polymerase in polymer formation. Evidence for active site similarities to the ADP-ribosylating toxins. *J. Biol. Chem.* **270**, 3247–3254 (1995).
22. F. W. Farley, P. Soriano, L. S. Steffen, S. M. Dymecki, Widespread recombinase expression using FLPeR (flipper) mice. *Genesis* **28**, 106–110 (2000).
23. B. P. Zambrowicz *et al.*, Disruption of overlapping transcripts in the ROSA beta geo 26 gene trap strain leads to widespread expression of beta-galactosidase in mouse embryos and hematopoietic cells. *Proc. Natl. Acad. Sci. U.S.A.* **94**, 3789–3794 (1997).
24. X. S. Wang, B. J. Lee, S. Zha, The recent advances in non-homologous end-joining through the lens of lymphocyte development. *DNA Repair (Amst)* **94**, 102874 (2020).
25. G. Li *et al.*, Lymphocyte-specific compensation for XLF/cernunnos end-joining functions in V(D)J recombination. *Mol. Cell* **31**, 631–640 (2008).
26. L. Liu *et al.*, Autophosphorylation transforms DNA-PK from protecting to processing DNA ends. *Mol. Cell* **82**, 177–189.e4 (2022).
27. M. E. Moynahan, J. W. Chiu, B. H. Koller, M. Jasin, Brca1 controls homology-directed DNA repair. *Mol. Cell* **4**, 511–518 (1999).
28. A. Gunn, J. M. Stark, I-SceI-based assays to examine distinct repair outcomes of mammalian chromosomal double strand breaks. *Methods Mol. Biol.* **920**, 379–391 (2012).
29. K. Yamamoto *et al.*, Kinase-dead ATM protein is highly oncogenic and can be preferentially targeted by Topo-isomerase I inhibitors. *Elife* **5**, e14709 (2016).
30. E. Rass, G. Chandramouly, S. Zha, F. W. Alt, A. Xie, Ataxia telangiectasia mutated (ATM) is dispensable for endonuclease I-SceI-induced homologous recombination in mouse embryonic stem cells. *J. Biol. Chem.* **288**, 7086–7095 (2013).
31. E. M. Kass *et al.*, Double-strand break repair by homologous recombination in primary mouse somatic cells requires BRCA1 but not the ATM kinase. *Proc. Natl. Acad. Sci. U.S.A.* **110**, 5564–5569 (2013).
32. S. J. Pettitt *et al.*, Genome-wide and high-density CRISPR-Cas9 screens identify point mutations in PARP1 causing PARP inhibitor resistance. *Nat. Commun.* **9**, 1849 (2018).
33. H. Schuhwerk *et al.*, Kinetics of poly(ADP-ribosyl)ation, but not PARP1 itself, determines the cell fate in response to DNA damage in vitro and in vivo. *Nucleic Acids Res.* **45**, 11174–11192 (2017).
34. M. J. Suskiewicz *et al.*, HPF1 completes the PARP active site for DNA damage-induced ADP-ribosylation. *Nature* **579**, 598–602 (2020).
35. D. Menolfi, S. Zha, ATM, ATR and DNA-PKcs kinases-the lessons from the mouse models: Inhibition not equal deletion. *Cell Biosci.* **10**, 8 (2020).
36. Z. Shao *et al.*, DNA-PKcs has KU-dependent function in rRNA processing and haematopoiesis. *Nature* **579**, 291–296 (2020).
37. X. S. Wang *et al.*, DNA damage-induced phosphorylation of CtIP at a conserved ATM/ATR site T855 promotes lymphomagenesis in mice. *Proc. Natl. Acad. Sci. U.S.A.* **118**, e2105440118 (2021).
38. S. Zha, J. Sekiguchi, J. W. Brush, C. H. Bassing, F. W. Alt, Complementary functions of ATM and H2AX in development and suppression of genomic instability. *Proc. Natl. Acad. Sci. U.S.A.* **105**, 9302–9306 (2008).
39. S. Zha, F. W. Alt, H. L. Cheng, J. W. Brush, G. Li, Defective DNA repair and increased genomic instability in Cernunnos-XLF-deficient murine ES cells. *Proc. Natl. Acad. Sci. U.S.A.* **104**, 4518–4523 (2007).
40. F. Dantzer *et al.*, Poly(ADP-ribose) polymerase-2 contributes to the fidelity of male meiosis I and spermiogenesis. *Proc. Natl. Acad. Sci. U.S.A.* **103**, 14854–14859 (2006).